Mon. Not. R. Astron. Soc. **000**, 1–13 (2010) Printed December 20, 2010 (MN LATEX style file v2.2)

# Lucky Imaging Adaptive Optics of the brown dwarf binary GJ569Bab⋆

B. Femenía[1,2]†, R. Rebolo[1,3], J. A. Pérez-Prieto[1], S. R. Hildebrandt[1,4], L. Labadie[1,2], A. Pérez-Garrido[5], V. J. S. Béjar[1,2], A. Díaz-Sánchez[5], I. Villó[5], A. Oscoz[1], R. López[1], L. F. Rodríguez[1] and J. Piqueras[1,6]

[1]*Instituto de Astrofísica de Canarias, C/ Vía Láctea S/N, E-38200 La Laguna, Spain*
[2]*Departamento de Astrofísica, Universidad de La Laguna, E-38205 La Laguna, Tenerife, Spain*
[3]*Consejo Superior de Investigaciones Científicas, Spain*
[4]*Laboratoire de Physique Subatomique et Cosmologie, F-38000 Grenoble, France*
[5]*Universidad Politécnica de Cartagena, Campus Muralla del Mar, Cartagena, Murcia E-30202, Spain*
[6] *Max-Planck-Institut für Sonnensystemforschung, Max-Planck-Str. 2, D-37191 Katlenburg-Lindau, Germany*

Accepted 2010 December 16. Received 2010 December 15; in original form 2010 August 2

**ABSTRACT**

The potential of combining Adaptive Optics (AO) and Lucky Imaging (LI) to achieve high precision astrometry and differential photometry in the optical is investigated by conducting observations of the close 0.″1 brown dwarf binary GJ569Bab. We took 50000 *I*-band images with our LI instrument FastCam attached to NAOMI, the 4.2-m William Herschel Telescope (WHT) AO facility. In order to extract the most of the astrometry and photometry of the GJ569Bab system we have resorted to a PSF fitting technique using the primary star GJ569A as a suitable PSF reference which exhibits an *I*-band magnitude of $7.78 \pm 0.03$. The AO+LI observations at WHT were able to resolve the binary system GJ569Bab located at $4.''92 \pm 0.''05$ from GJ569A. We measure a separation of $98.4 \pm 1.1$ mas and *I*-band magnitudes of $13.86 \pm 0.03$ and $14.48 \pm 0.03$ and $I - J$ colors of 2.72±0.08 and 2.83±0.08 for the Ba and Bb components, respectively. Our study rules out the presence of any other companion to GJ569A down to magnitude I∼ 17 at distances larger than 1″. The $I - J$ colors measured are consistent with M8.5-M9 spectral types for the Ba and Bb components. The available dynamical, photometric and spectroscopic data are consistent with a binary system with Ba being slightly (10-20%) more massive than Bb. We obtain new orbital parameters which are in good agreement with those in the literature.

**Key words:** Instrumentation: high angular resolution - Instrumentation: adaptive optics - Stars: low-mass, brown dwarfs - Binaries: close - Stars:individual: GJ569

## 1 INTRODUCTION

The lucky imaging (LI) technique proposed by Fried (1978) attracted the attention by professional astronomers once low read-out noise detectors became available (e.g. Baldwin et al. 2001; Tubbs et al. 2002; Law et al. 2006). Recently it has been realized that the combination of LI and Adaptive Optics (AO) can benefit mutually and provide high-resolution imaging close to the diffraction limit at optical and near-infrared (NIR) wavelengths (e.g. see Gladysz et al. 2008; Law et al. 2009; Kervella et al. 2009). This can be obtained by using a larger fraction of data in the LI selection and/or keeping images with a better Strehl ratio than in conventional LI observations.

In this paper we present the results of combining the LI and AO techniques to produce high-angular resolution and high-contrast imaging in the optical of the multiple system GJ569Bab which is a benchmark in the study and characterization of brown dwarfs (BDs). GJ569A is an M2.5V cromospherically active star lying at a distance of 9.6-9.8 pc (Perryman et al. 1997; van Leeuwen 2007). Forrest et al. (1988) identified a faint companion to GJ569 and argued the potential brown dwarf nature of such companion. Using Keck AO observations Martín et al. (2000) resolved GJ569B as a binary brown dwarf system with a separation of $\sim 0.''1$, a total mass of the system in the range 0.09-0.15 $M_{\odot}$ , an age in the

⋆ Based on service observations made with the WHT telescope operated on the island of La Palma by the Isaac Newton Group and on observations made with the Nordic Optical Telescope, operated on the island of La Palma jointly by Denmark, Finland, Iceland, Norway, and Sweden, in the Spanish Observatorio del Roque de los Muchachos of the Instituto de Astrofísica de Canarias.

† E-mail:bfemenia@iac.es

range 0.12-1.0 Gyr and an orbital period ~ 3 yr. Further AO-based observations with the Keck telescope (e.g. Lane et al. 2001; Zapatero Osorio et al. 2004; Simon et al. 2006; Konopacky et al. 2010) and the Subaru and HST telescopes (Zapatero Osorio et al. 2005; Martín et al. 2006) have allowed precise determination of the dynamical masses and orbital parameters of the binary system GJ569Bab (see Table 7 in this paper) as well as a precise determination of the spectral types of the GJ569B components: M8.5-9V and M9V for the Ba and Bb components, respectively (Lane et al. 2001; Martín et al. 2006).

For BDs an estimate of the mass is essential to determine their properties and evolution. A way to achieve a direct measurement of masses is to observe close binary systems where the short orbital period allows for a complete sampling of the orbit and from here a precise determination of the dynamical masses of the pair. Up to now a complete characterization of the orbital motion has been achieved for a few BD binaries (e.g. see Dupuy et al. 2009; Konopacky et al. 2010). In this context GJ569Bab constitutes a unique laboratory where to test the stellar evolutionary models as it is among the shortest known period BD binary system. This has allowed to determine the orbit of the system over several periods and from here a precise determination of its dynamical mass.

The high angular resolution requested to spatially resolve faint systems like GJ569B into its components has been so far achieved with 10-m class telescopes and AO in the NIR or with the HST.. Our motivation to perform observations of GJ569 with LI+AO on a 4-m class telescope was twofold. First, to test the potential of this technique for high-angular resolution and high-contrast imaging in the optical regime. Second, to shed light on whether GJ569B is actually a triple system as suggested in some works in the literature (Martín et al. 2000; Kenworthy et al. 2001; Simon et al. 2006).

In Section 2 we briefly describe the instrumental set-up. Section 3 describes the observations. Section 4 reports the data calibration, reduction and analysis. Section 5 focuses on the photometry and astrometry of the GJ569 system components and discussion of the results. We provide our conclusions in Sect. 6.

## 2 INSTRUMENTAL SETUP.

FastCam is a LI-based instrument developed jointly by the Instituto de Astrofísica de Canarias (IAC) and Universidad Politécnica de Cartagena (UPCT). In brief, FastCam consists of a commercial Electro Multiplying Charge Coupled Device (EMCCD), a very simple versatile optics setup offering different plate scales to be accommodated at different telescopes configurations and an FPGA-based[1] on-line processing and acquisition hardware. Its high degree of versatility has allowed us to collect images on a wide range of telescopes with diameters from 1.5 to 4.2 m. Further details of the FastCam instrument and results achieved so far at different telescopes are presented in Oscoz et al. (2008); Labadie et al. (2010).

The observations reported in this paper were acquired at the 4.2 meter William Herschel Telescope (WHT) at Observatorio del Roque de Los Muchachos (ORM, La Palma). FastCam was installed at NAOMI, the AO facility at WHT. It suffices here to say it is an AO system based on a $8\times8$ subaperture Shack-Hartmann sensor and the most prominent feature of the system is the use of a fully segmented deformable mirror. Details for NAOMI can be found in Myers et al. (2003); Benn (2006). We also resorted to non-AO LI observations with FastCam at the Cassegrain focus of the Nordic Optical Telescope (NOT) at the ORM mainly for plate scale and orientation calibration.

The standard data acquisition of FastCam is that raw data are composed of cubes of 1000 images each. The full detector of FastCam is an E2V EMCCD with 512×512 pixels (commercial camera model Andor iXon DU-987) exhibits a maximum frame rate of 35 Hz, although the exposure time for each individual frame can be set at values shorter than 1/35 seconds but at the cost of incurring on overheads.

## 3 OBSERVATIONS.

### 3.1 AO+LI observations with the WHT telescope.

On the 4th of June 2009 FastCam was configured for an individual frame exposure time of 30 msec and with optics providing a field of view for FastCam of 7×7 arcsec$^2$ (see Section 4.1.3). The primary star GJ569A was used as the guide star for both the NAOMI and the FastCam real-time selection algorithm. Such real-time selection is performed by the FPGA-based acquisition system and it is mostly used to detect any anomalies or malfunctioning of the system by displaying the best 10% frames based on the brightest pixel selection although the entire frame set is kept for off-line processing. With this FastCam configuration, we collected 50 cubes which amount to a total exposure time of 1500 seconds in the standard I Johnson-Bessell band (872.2 nm central wavelength, 298 nm FWHM) and 824 nm central wavelength, 175 nm FWHM when the EMCCD QE curve is considered. Taking into account overheads, the total time spent on GJ569 was 2340 seconds. During most of the observation time on GJ569 we had access to the RoboDIMM[2] seeing monitor which reported an average seeing in the visible of $0\farcs49 \pm 0\farcs08$ (minimum seeing $0\farcs38$, maximum seeing $0\farcs77$) during the observation of GJ569. We also observed astrometric binaries for plate scale and orientation calibration (see Section 4.1.2).

### 3.2 LI observations with the NOT telescope.

On the 24th July 2008 FastCam was configured for an individual frame exposure time of 20 msec and with optics providing a field of view for FastCam of 16×16 arcsec$^2$ (see Section 4.1.1). In the I Johnson-Bessell band (same filter as with the WHT, see Section 3.1) we collected 10 cubes which correspond to a total exposure time of 200 seconds. No independent measurements for the seeing conditions were available at the time although the combined image of all 10000 individual frames yields an estimate for the seeing of $\sim 0\farcs5$ at the detector plane. The primary star GJ569A was used as the guide star for the FastCam real-time selection algorithm. We also observed the M15 globular cluster for plate scale and orientation calibration (see Section 4.1.1).

### 3.3 Observations with the IAC80 telescope.

For photometric calibration purposes we obtained *I*-band images of GJ569 on April 6 2010 using the CAMELOT instrument mounted on the IAC80 telescope with an identical filter to the ones used in Sections 3.1 and 3.2. CAMELOT consists of a 2K×2K CCD detector with a 0.304"/pix plate scale providing a field of view of

[1] FPGA, Field Programmable Gate Arrays

[2] `http://www.ing.iac.es/Astronomy/development/seeing/Correl_DIMM.html`

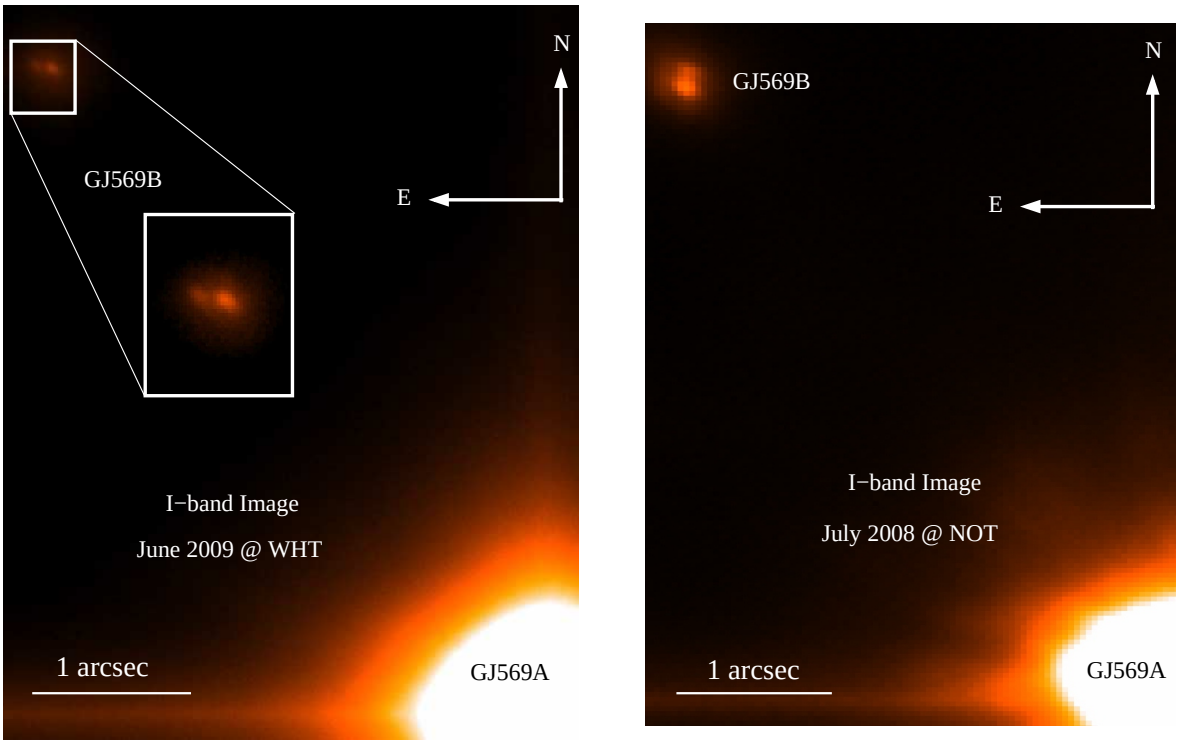


**Figure 1.** Left: I-band image of GJ569 observed on the 4th of June 2009 with FastCam at the science focus of the WHT telescope AO system. Right: GJ569 in the I-band observed on the 24th of July 2008 with the NOT telescope. The image at the WHT is clearly resolved into the GJ569Ba and GJ569Bb components, while the NOT image acquired nearly 1 year before suggests a binary system because of the elongation of GJ569B. Both images have been rotated by their respective Position Angle Offsets (see Section 4.1 to have the North and East axis pointing upwards and to the left, respectively).

10.4×10.4 arcmin$^2$. We observed a series of 10 images with individual exposure time of 5s. Raw data were reduced using routines within the IRAF environment [3]. Images bias was subtracted using the overscan region and zero exposure time images. The flat field correction made use of dome flats. Aperture photometry was performed using routines within the DAOPHOT package. Weather conditions during our observations were photometric and average seeing ranged from 1.3 to 2". Instrumental magnitudes were transformed into apparent magnitudes in the Johnson-Bessel system using photometric standard stars from Landolt (1992) obtained at different airmasses before and after our science target. Since images of GJ569 were defocused to avoid saturation, aperture correction was applied to the photometry of the standards to match the larger aperture used for our object. From these data, we have measured that the *I*-band magnitude of GJ569A is 7.78±0.03.

## 4 DATA REDUCTION AND ANALYSIS

The image selection employed is the same as with non-AO observations (Oscoz et al. 2008; Labadie et al. 2010) which selects the best images as those exhibiting the largest ratio between the brightest pixel in the image and the rms of the overall image. The images are sorted out from best to worst image according to the brightest pixel criterion with a very small fraction of individual frames exhibiting saturated pixels (due either to cosmic rays or spurious electronic events) removed. Then the user defines the percentage of best images to be kept on which a shift-and-add algorithm is applied. Standard image reduction considered only bias subtraction as experience with the FastCam EMCCD has revealed its excellent cosmetic and no need for flat fielding. Bias subs-traction, image selection and shift-and-add algorithm are performed using our own software.

### 4.1 Plate Scale and Orientation Calibration

#### *4.1.1 NOT calibration with M15*

As part of the observation program with the NOT telescope on the night of 24th July 2008, we also conducted observations of the M15 globular cluster which, besides its specific science case, constitutes a very precise astrometric calibrator yielding a plate scale accuracy of a few tens of microarcseconds and plate orientation below $0.^\circ1$ when the FastCam image of the M15 core is compared against HST WFPC2 images of M15 (van der Marel et al. 2002). For the instrumental setup on the 24th of July 2008 we measured a plate scale of $31.176 \pm 0.030$ mas and a Position Angle (P.A.) offset of $-89.84^\circ \pm 0.05^\circ$ (i.e. North axis is at $89.84^\circ$ clockwise from CCD y-axis).

#### *4.1.2 WHT calibration with WDS binaries.*

Observations of the M15 globular cluster were not possible on June 2009 as none of the cluster stars is bright enough for efficiently locking the NAOMI loop. Because of this we observed four astrometric binaries (HD98231, HD105824, HD186858, HD197913)

[3] IRAF is distributed by National Optical Astronomy Observatories, which is operated by the Association of Universities for Research in Astronomy, Inc., under contract to the National Science Foundation.

selected from the Washington Double Star (WDS) Catalog (Wycoff et al. 2006) with an adequate component separation and brightness to act as astrometric calibrators. The calibration achieved from the WDS binaries (HD98231, HD105824, HD186858, HD197913) yields a plate scale of $13.63 \pm 0.23$ mas and a Position Angle Offset of $91.3° \pm 0.9°$. The uncertainties assigned from the WDS astrometry corresponds to the dispersion of the values from each of the WDS binaries.

#### *4.1.3 WHT calibration with GJ569.*

We are able to compute the GJ569B photocentre position with respect to GJ569A with high accuracy at the NOT image on July 24th 2008 (see Table 5). The orbital period of GJ569B around GJ569A is known a priori to be very long. With the information in Table 5 we predict the coordinates of GJ569B with respect to GJ569A on June 4th 2009 (WHT observation) implicitly dismissing GJ569A-B orbital displacements between the images at the NOT and at the WHT nearly one year later. From here a plate scale of $13.40 \pm 0.14$ mas and a Position Angle Offset of $91.8° \pm 0.6°$ is derived. A weighted average of these values with those obtained in Section 4.1.2 yields the calibration assumed in this work for the WHT data: $13.46 \pm 0.12$ mas and $91.6° \pm 0.5°$ for the plate scale and Position Angle, respectively.

### 4.2 PSF of the observations.

The NAOMI system is optimized to deliver well corrected wavefronts above 1.0 $\mu$m, while in the optical the aim is not to deliver well corrected images (i.e. with a significant Strehl ratio) but simply to achieve a reduction by a factor 2 of the FHWM with respect to the seeing-limited images. The combination of AO+LI allows to achieve FHWM reductions by at least a factor 5 with respect to the seeing-limited images as shown in Fig. 2 and Fig. 3 where we show the evolution of the FWHM and different cuts of the PSF versus the LI % selection, respectively. The PSF cuts shown in Fig. 3 correspond to the PSF as measured on GJ569A for both the NOT and the WHT images.

The FWHM evolution depicted in Fig. 2 shows the usual low sensitivity of the FWHM upon LI %, a trend already pointed out in previous works (e.g. see Law et al. 2009). To understand this trend one must take into account that most of the turbulence is concentrated in the tip-tilt modes which are removed in the LI scheme, while higher-order turbulent modes tend to distort the PSF but without enlarging it significantly. The effect of these higher-order modes in the PSF can be understood as a leak of power towards outside the PSF core, giving rise to the familiar LI PSFs consisting on a very well defined narrow core on top of a much wider and swallower halo. Qualitatively one can think that the better the AO correction or the most stringent the LI frame selection are, the more prominent the core over the halo becomes. This is in fact what we observe in the PSF cuts in Fig. 3, where the PSFs have been normalized to have unit volume. In this way we notice that when we restrict ourselves to very low LI % selection the PSF peaks much higher with respect to the halo that when using a larger LI % selection. This leads directly to a trade-off when having to decide the frame % to keep when one also considers the desirable SNR to achieve.

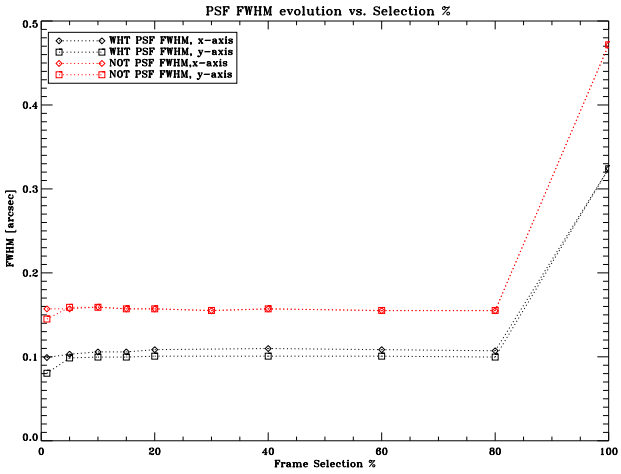


**Figure 2.** Evolution of the PSF FWHM at NOT (red) and WHT(black) as a function of the percentage of images kept in the selection procedure. The PSF is directly the image of GJ569A. In this plot the x-axis corresponds to the direction at which the PSF is widest and the y-axis is perpendicular to the x-axis. Notice these x and y axes do not necessarily correspond to the CCD x and y axes. The asymmetry of the PSF for the WHT observations is believed to be caused by the absence of an atmospheric dispersion corrector.

### 4.3 The PSF fitting technique

In order to perform an estimate of the relative photometry and astrometry between the primary component and each of the resolved components of GJ569B we have resorted to a Levenberg-Marquadt (LM) non-linear least-squares (Bevington 1992) PSF fitting algorithm[4]. We assume the PSF measured at the GJ569A location and the PSF at GJ569B position do not differ significantly. This is justified by the excellent seeing conditions experienced during the observations and the fact that the isoplanatic angle at the ORM at 820 nm is frequently larger than the 5 arcsec separation between GJ569A and B (see e.g. Fuensalida et al. 2004; Law et al. 2006). It has also been pointed out by Law et al. (2006) that as the LI technique selects the best fraction of frames where the turbulence is smallest, it is expected that those frames also exhibit larger isoplanatic angles than would be observed in traditional long exposure imaging. Therefore, for a separation of about 5″we should be within the isoplanatic angle at $\sim$ 820 nm and the assumption of uniformity of the PSF at the GJ569A and GJ569B locations is well justified.

Our fitting model is applied to a relatively small box with only GJ569B and assumes the signal on each pixel in the box, $f(x,y)$, is due to two components GJ569Ba and G569Bb located at positions $(x_a,y_a)$ and $(x_b,y_b)$, respectively, and with fluxes $a$ and $b$ relative to the flux of GJ569A, plus a possible offset (OFF) associated either to sky background or a bias offset in the final image:

$$f(x,y) = a \cdot PSF(x-x_a, y-y_a) + b \cdot PSF(x-x_b, y-y_b) + \mathbf{OFF} \quad (1)$$

Note that in our LM PSF fitting scheme we do not fit an analytical PSF function nor attempt first a fit to the PSF measured at GJ569A. Instead we use directly the measured GJ569A PSF in the WHT image which is moved across a $100 \times 100$ pixel box by performing FFT-based shifts. In this way, the PSF fitting technique also provides us with a measurement of the distance between each

[4] Using the MPFIT toolset by C. Markwardt available at `http://cow.physics.wisc.edu/~craigm/idl/idl.html`

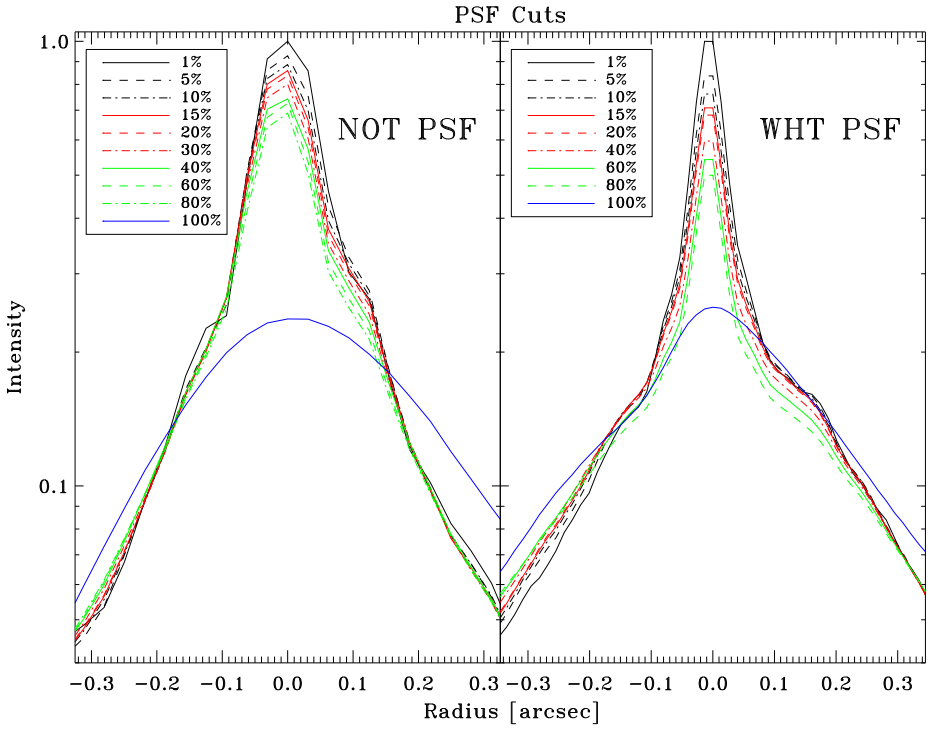


**Figure 3.** Cuts of the PSFs at the NOT and WHT as a function of the percentage of images kept in the selection procedure. The PSF is directly the image of GJ569A. The PSFs have been normalized so that the highest PSF exhibits peak unity and all of them have the same volume under the PSF.The gain in resolution from the WHT with respect to the NOT is due both to the increasing WHT diameter plus the use of the NAOMI system.Notice the blue line in the NOT plot represents the seeing-limited PSF while in the case of the the blue PSF in the WHT diagram corresponds to a partially tip-tilt removed by the NAOMI system.

of the GJ569B components with respect to each other and with respect to GJ569A.

The results of the LM PSF fitting technique on the image composed by the best 16% of the frames from the WHT observation are summarized in Table 1 for different values of the threshold background parameter ($\eta$). This parameter determines the number of pixels within the $100\times100$-pixel box which are finally considered in the fitting process: only those pixels exceeding the background level by a factor $\eta$ the rms background. Pixels below such threshold are shown in black in Fig. 4. As it can be seen in Table 1, when applied to the WHT image the technique is rather insensitive to the choice of pixels in the fitting (i.e. little sensitivity to the $\eta$ parameter) and provides the relative photometry with excellent accuracy.

For the PSF fitting model to work properly and provide with meaningful error bars, the pixels in the image have to be assigned realistic error bars. During the analysis of the data the simple choice whether a given pixel was background limited or source limited was not good enough. At this point it revealed particularly useful the fact that the LI scheme allows for a precise distribution of values of the signal for each pixel in the final image since we have access to all the individual frames. For the final WHT image made of the best 16% individual frames, the value assigned to each pixel is the mean of a distribution sampled with 8000 values and we also generated an error map computed as the error of the mean.

The LM PSF fitting technique was also robust versus the LI selection fraction, exhibiting little dispersion on the derived parameters as it is shown in Table 2 for the choice $\eta = 3.0$. The choice of the 16% fraction to generate the final LI image for the WHT data was based entirely on the value of the reduced $\chi^2$ achieved in this series of fits: the WHT image generated with a 16% of the best images exhibits $\chi^2/\nu = 1.04$ ($\nu$ being the number of degrees of freedom).

The case for the NOT image is less favourable. When applied to the NOT image the LM PSF fitting was not that robust and we believe this is due both to the lower number of images under consideration but mainly to the fact the blending of both sources hampers a good fit.

### 4.4 Detectability curves.

A key point to characterize the combination of AO-assisted LI systems for the detection of low-mass companions is the study of the detectability curves as a function of the distance to the star. This has been done in Fig. 5 where on the left panel we show the $3\sigma$ detectability curves for a variety of percentages of the images kept to generate the final images. On the right panel we have plotted the detectability curves on the same images upon filtering them with a wavelet transform algorithm. The details of this wavelet-based post-processing algorithm are described in Labadie et al. (2010) and the general purpose of such filtering technique is the increase in the contrast ratio achievable by suppressing the low-frequency halo of the primary star which hides the presence of much fainter companions (Masciadri & Raga 2004). Both sets of detectability curves were obtained as follows: at a given distance $\rho$ from the primary star we identify all possible sets of small boxes of size the FWHM of the PSF (i.e. $7\times7$ pixel boxes). Only regions of the image showing structures easily recognizable as spikes due to diffraction of the telescope spider and/or artifacts on the read-out of the detector are

**Table 1.** LM PSF fitting results on the WHT image from best 16% of frames.

| $\eta$ | $a\times10^3$ | $b\times10^3$ | $b/a$ | $\rho(mas)$ | P.A. (°) | $\chi^2/\nu$ |
|---|---|---|---|---|---|---|
| 2.0 | $3.743\pm0.023$ | $2.126\pm0.022$ | $0.568\pm0.009$ | $98.6\pm1.1$ | $78.0\pm0.7$ | 0.92 |
| 2.5 | $3.733\pm0.024$ | $2.113\pm0.023$ | $0.566\pm0.009$ | $98.6\pm1.1$ | $78.0\pm0.7$ | 0.95 |
| **3.0** | $\mathbf{3.715\pm0.024}$ | $\mathbf{2.096\pm0.023}$ | $\mathbf{0.564\pm0.009}$ | $\mathbf{98.4\pm1.1}$ | $\mathbf{78.0\pm0.7}$ | **1.04** |
| 3.5 | $3.689\pm0.024$ | $2.076\pm0.023$ | $0.563\pm0.009$ | $98.2\pm1.1$ | $78.0\pm0.7$ | 1.10 |
| 4.0 | $3.666\pm0.025$ | $2.054\pm0.024$ | $0.560\pm0.009$ | $97.8\pm1.1$ | $78.1\pm0.7$ | 1.16 |
| 5.0 | $3.626\pm0.026$ | $1.994\pm0.025$ | $0.550\pm0.009$ | $97.5\pm1.1$ | $78.2\pm0.7$ | 1.27 |
| 6.0 | $3.561\pm0.028$ | $1.920\pm0.026$ | $0.539\pm0.010$ | $96.8\pm1.1$ | $78.1\pm0.7$ | 1.33 |
| 7.0 | $3.490\pm0.029$ | $1.821\pm0.028$ | $0.522\pm0.010$ | $95.8\pm1.2$ | $78.1\pm0.7$ | 1.25 |

**Table 2.** LM PSF fitting results as a function of the percentage of frames kept to generate the WHT image.

| LI % | $a\times10^3$ | $b\times10^3$ | $b/a$ | $\rho(mas)$ | P.A. (°) | $\chi^2/\nu$ |
|---|---|---|---|---|---|---|
| 1 | $3.35\pm0.06$ | $1.77\pm0.05$ | $0.528\pm0.021$ | $96.5\pm1.8$ | $77.8\pm1.1$ | 0.880 |
| 5 | $3.59\pm0.05$ | $2.07\pm0.04$ | $0.576\pm0.018$ | $98.1\pm1.5$ | $78.2\pm0.9$ | 0.360 |
| 10 | $3.688\pm0.029$ | $2.082\pm0.026$ | $0.565\pm0.010$ | $98.5\pm1.2$ | $78.2\pm0.7$ | 0.722 |
| **16** | $\mathbf{3.715\pm0.024}$ | $\mathbf{2.096\pm0.023}$ | $\mathbf{0.564\pm0.009}$ | $\mathbf{98.4\pm1.1}$ | $\mathbf{78.2\pm0.6}$ | **1.04** |
| 20 | $3.710\pm0.022$ | $2.125\pm0.021$ | $0.573\pm0.008$ | $98.3\pm1.1$ | $78.0\pm0.6$ | 1.27 |
| 40 | $3.745\pm0.017$ | $2.148\pm0.016$ | $0.574\pm0.006$ | $98.3\pm1.0$ | $78.3\pm0.6$ | 2.11 |
| 60 | $3.765\pm0.015$ | $2.140\pm0.014$ | $0.569\pm0.005$ | $98.9\pm1.0$ | $78.2\pm0.6$ | 2.77 |
| 80 | $3.755\pm0.014$ | $2.132\pm0.013$ | $0.568\pm0.005$ | $98.6\pm1.0$ | $78.1\pm0.5$ | 3.24 |

not considered. For each of the valid boxes on the arc at distance $\rho$ the standard deviation of the image pixels within the 7-pixel boxes is computed. The value assigned to the $3\sigma$ detectability curve at distance $\rho$ is 3 times the mean value from the standard deviations of all the eligible boxes at distance $\rho$ from GJ569A. From the curves in both panels in Fig. 5 we notice the following behaviours:

(i) On the non-wavelet filtered image, at short distances ($< 1\farcs5$) from the primary star, the lower the fraction of data used the higher the detectability gain is with a maximum gain of around $\sim 0.9$ magnitudes between the 80% and 1% frame selection. This improvement in contrast is due a slightly better angular resolution with a very restrictive frame selection. As we move away from the primary star, the detectability curves approach to each other until eventually the situation is reversed. At large distances the image is dominated by background/detector noise so that the higher the percentage of frames used to generate the image, the deeper the detectability curve gets.

(ii) On the wavelet-processed image there is no transition between the inner region (i.e separation from primary below $1\farcs5$) and the outer region. The detectability at the inner regions is always improved with respect to the non-processed image and, in addition, the higher the percentage of data kept for the image, the deeper the detectability gain. Above $1\farcs5$ separation from the primary star, there is no real difference between the detectability achieved on the original and the wavelet-processed image, as it is expected at those regions of the image which are dominated by background/detector noise which can not be removed by the wavelet post-processing technique.

## 5 RESULTS.

### 5.1 Photometry of the GJ569 system.

The final $I$-band differential magnitudes ($\Delta m_{AB} = m_B - m_A$) derived by the LM PSF fitting technique described in Section 4.3 are summarized in Table 3. The magnitude difference between GJ569Ba and GJ569Bb we find is very similar to the 0.7 mag found by Martín et al. (2006) using the F814W filter in the HST which resembles the $I$-band. These values are slightly larger than the 0.5 magnitude difference measured in the $J,H$ and $K$-band by Martín et al. (2000). All these data are consistent with the spectral determination of M8.5-M9 for the brown dwarf binary derived in the near-infrared by Lane et al. (2001). However, given the uncertainties, we can not discard that both components have a similar spectral type of M9, as obtained by Martín et al. (2006) using optical spectra.

**Table 3.** Differential magnitudes in I band with FastCam at WHT

| | |
|---|---|
| $\Delta m_{AB}$ | $5.590\pm0.004$ |
| $\Delta m_{ABa}$ | $6.075\pm0.007$ |
| $\Delta m_{ABb}$ | $6.697\pm0.012$ |
| $\Delta m_{BaBb}$ | $0.622\pm0.017$ |

Using the $I$-band photometry obtained in the IAC80 for GJ569A (see Section 3.3), and the differential magnitude between the primary and the brown dwarf binary found with FastCam (see Table 3), we derived an integrated photometry of $I$=13.37±0.03 for GJ569B with the WHT image and $I$=13.41±0.03 with the NOT image. As remarked previously, the lack of enough spatial resolution on the NOT image does not allow to resolve the GJ569B binary system, but aperture photometry of the whole GJ569B system is compatible with what we derive from the LM PSF fitting of the WHT image. This value is not in good agreement with the previous result by Forrest et al. (1988) ($I$=13.88±0.2), probably affected by the contamination of the primary. To check a possible variability of GJ569A , we have compared the apparent magnitude of this object and the G1V star HD130948, which was observed during the same nights in the IAC80 and the NOT. We have found no relative difference in their $I$-band magnitude at the level of a few tens of

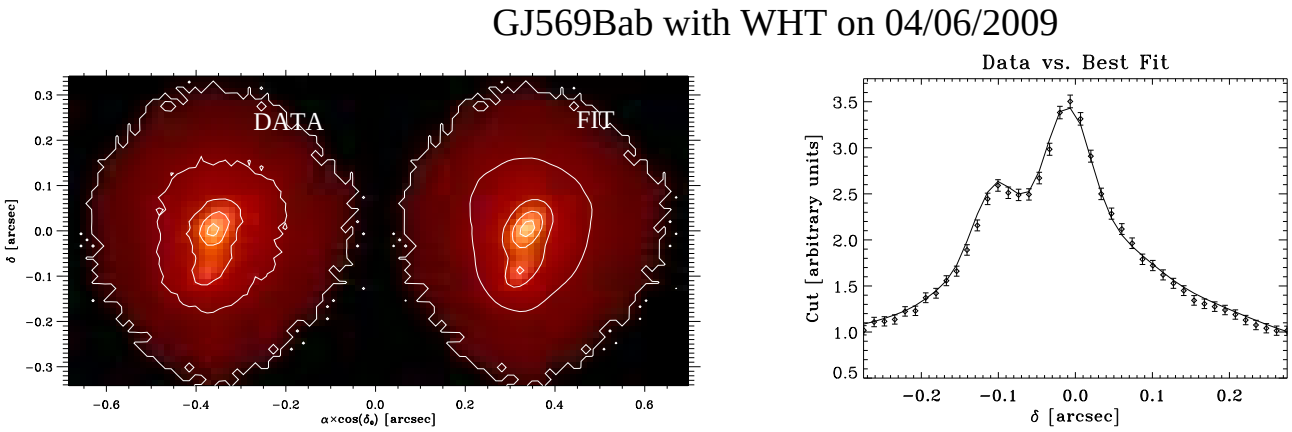


**Figure 4.** Comparison of actual images to best fit models and respective cuts along lines joining GJ569Ba to GJ569Bb for data acquired with the WHT on 4/6/2009. The oversampling of the WHT data and a better PSF due to the use of the AO facility at the WHT allows to resolve the binary nature of GJ569B allowing the LM PSF fitting technique to achieve a good fit to the data. On both images dark areas indicate regions whose pixels are not sufficiently above the background threshold to be taken into consideration in the PSF fitting (e.g. $\eta$ parameter in Tables 1 and 2). No rotation to align the North and East axis with the usual y and negative axes has been applied to the image.

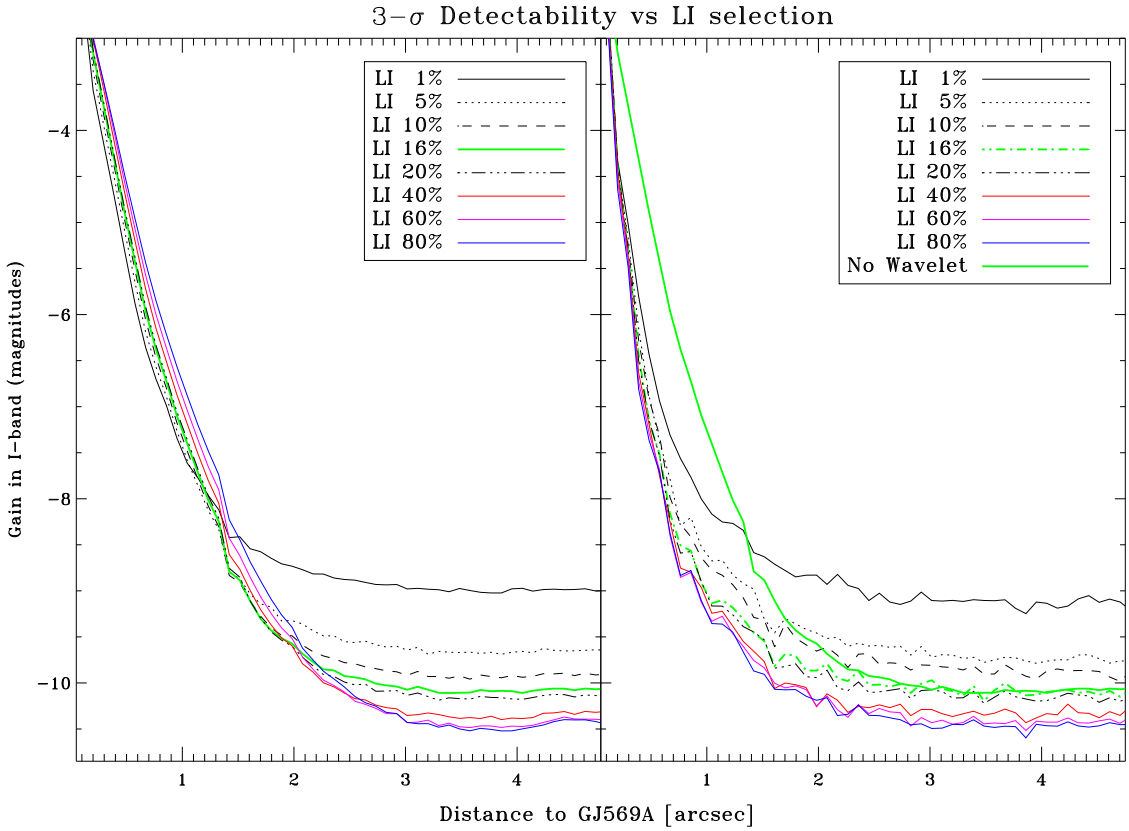


**Figure 5.** Evolution of the 3$\sigma$ detectability versus the percentage of images kept to generate the LI image. The left panel shows the 3$\sigma$ detectability curves obtained directly from the image. Right panel shows the 3-$\sigma$ detectability curve upon filtering with wavelets (see main text). The green thick solid lines in both plots correspond to a selection of the best 16 % frames without wavelet filtering and is displayed in the right panel for comparison purposes. Notice the big improvement by the wavelet filtering at angular distances below 1.″5, a slight gain at angular distances in the range [1.″5, 2″] and no net gain beyond 2″.

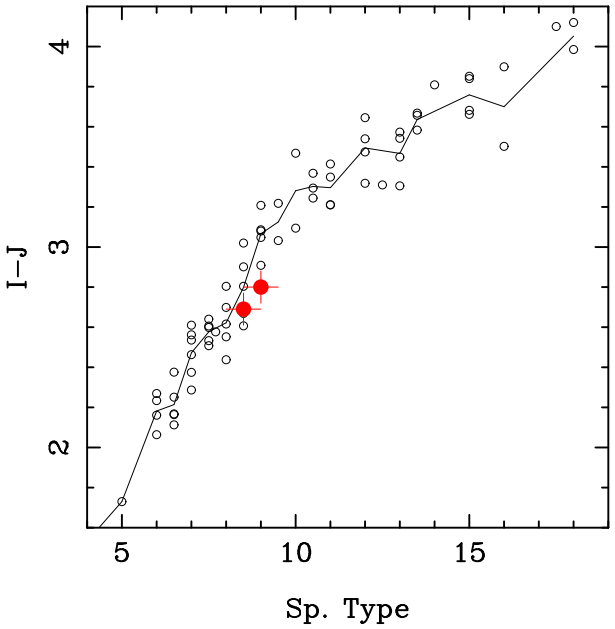


**Figure 6.** $I-J$,spectral type diagram of GJ569Ba and GJ569b (solid red circles) in comparison with M (M5 to M9 correspond to x-axis values 5 to 9) and L field dwarfs (L0 to L8 correspond to x-axis values 10 to 18) from Liebert & Gizis (2006) (open circles). The average color of these field dwarfs with the same spectral type are indicated by the solid line. The $J$-ban photometry obtained from Lane et al. (2001) in the CIT system has been transformed into the 2MASS system using the relations in Carpenter (2001).

millimagnitudes. The absolute photometry of both components of the brown dwarf binary was conducted in a similar way and a summary with the apparent magnitudes as derived from this work and in the literature is given in Table 4.

With the $J$-band photometry in Lane et al. (2001) we derived a $I-J$ color of 2.72±0.08 and 2.83±0.08 for GJ569Ba and GJ569Bb, respectively. In Fig. 6 we show the $I-J$ color of both components in comparison with M and L field dwarfs of the same spectral type from Liebert & Gizis (2006). We have adopted the spectral determination of M8.5-M9 for the brown dwarf binary derived in the near-infrared by Lane et al. (2001). From this figure we can see that our estimated $I-J$ colors are in good agreement with these spectral types.

According to the absolute magnitudes and colors of field dwarfs (Kirkpatrick & McCarthy 1994; Liebert & Gizis 2006), we expect a relative magnitude difference of ∼ 0.4 mag in the $I$-band, and a $I-J$ color difference of 0.27±0.22 for a M8.5/M9. All these data are also consistent with previous determinations of spectral types, in particular for those deriving a slightly earlier spectral type for GJ569Ba than for the Bb component.

### 5.2 Astrometry of GJ569A-GJ569B.

The compilation of all astrometric data on the GJ569B orbit around GJ569A, including our new measurement from the NOT observation, is provided in Table 5 and shown in Fig. 7 with the value obtained in this work in red. The higher accuracy of our measurement is immediately noticeable and it is due to the very precise image statistics combined with the high angular resolution PSFs provided by the LI technique and a very accurate NOT plate calibration, as discussed in Section 4.1.

**Table 5.** Astrometry of the binary system GJ569A-GJ569B.

| Date | Ref. | Separation (arcsec) | PA (°) |
|---|---|---|---|
| 1985 Jul 28 | [a] | 5.07 ± 0.15 | 17.4 ± 1.7 |
| 1987 Sep 18 | [a] | 5.01 ± 0.15 | 17.3 ± 1.7 |
| 1999 Aug 29 | [b] | 5.00 ± 0.05 | 25.0 ± 0.9 |
| 2001 Feb 8 | [c] | 4.89 ± 0.04 | 30 ± 3 |
| 2005 Feb 25 | [d] | 4.99 ± 0.19 | 33.1 ± 1.9 |
| 2008 Jul 24 | [e] | 4.94 ± 0.04 | 34.90 ± 0.05 |

References: [a]Forrest et al. (1988); [b]Martín et al. (2000); [c]Lane et al. (2001);[d]Simon et al. (2006); [e]This work

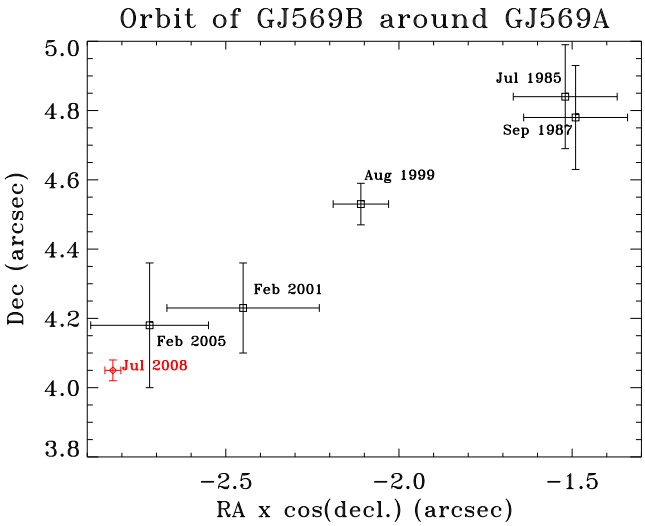


**Figure 7.** Compilation of positions of GJ569B on its long-period orbit around GJ569A using measurements in Table 5 and our point in red. GJ569A would be located at coordinates (0,0), which falls on purpose outside of the plot in order to make visible all points with their respective uncertainties.

Only the photocentre positions in Forrest et al. (1988) and in this work correspond to observations in the I band, while the rest of the observations have been conducted in the NIR. Since the flux ratios between the GJ569B components differ slightly from the NIR to the I-band measurement, we realize there might be a slight bias in the photocentre determination. In principle such a bias could be avoided by a proper weighting with the individual masses of the GJ569B pair, but due to the uncertainties in the individual GJ569Ba and GJ569Bb masses, the estimate of the barycenter remains essentially the same as the computation of the photocentre. The limited coverage of the GJ569B orbit around GJ569A (see Fig. 7) does not allow for a reliable orbit computation but still we estimate a low eccentricity long-period orbit of ∼400 years with a semi-major axis of 4.″3.

### 5.3 Orbital analysis of the GJ569B system.

As discussed in Section 4.3, the LM PSF fitting procedure applied to the WHT images allows us to obtain with high precision the relative position of Bb with respect to Ba (see Table 6). The same PSF fitting approach applied to the unresolved GJ569B NOT image delivers a relative astrometry for these two components with higher

**Table 4.** Updated compilation of GJ569 photometry.

| | Spec. Type | V magnitude | I magnitude | J magnitude | H magnitude | K magnitude |
|---|---|---|---|---|---|---|
| GJ569A | M2.5V[(d)] | 10.11†[(b)] | $7.78 \pm 0.03$[(j)] | $6.633 \pm 0.023$[(e)] | $5.990 \pm 0.021$[(e)] | $5.770 \pm 0.018$[(e)] |
| GJ569B | | | $13.88 \pm 0.2$[(a)] | $10.61 \pm 0.05$[(d)] | $10.16 \pm 0.10$[(a)] | $9.56 \pm 0.10$[(a)] |
| | | | $13.37 \pm 0.03$*[(j)] | $10.75 \pm 0.06$[(i)] | $10.15 \pm 0.04$[(i)] | $9.45 \pm 0.05$[(d)] |
| | | | $13.41 \pm 0.03$**[(j)] | | | $9.62 \pm 0.03$[(i)] |
| GJ569Ba | M8.5-9V[(d,f)] | | $13.86 \pm 0.03$[(j)] | $11.14 \pm 0.07$[(d)] | $10.43 \pm 0.04$[(g)] | $10.02 \pm 0.08$[(d)] |
| | | | | $11.18 \pm 0.08$[(f)] | | $9.86 \pm 0.10$[(g)] |
| GJ569Bb | M9V[(d,f)] | | $14.48 \pm 0.03$[(j)] | $11.65 \pm 0.07$[(d)] | $11.04 \pm 0.05$[(g)] | $10.43 \pm 0.08$[(d)] |
| | | | | $11.69 \pm 0.08$[(f)] | | $10.39 \pm 0.06$[(g)] |
| Bb/Ba | | | $0.70 \pm 0.23$‡[(f)] | $0.5 \pm 0.2$[(c)] | $0.5 \pm 0.1$[(c)] | $0.5 \pm 0.1$[(c)] |
| | | | $0.622 \pm 0.017$[(j)] | $0.51 \pm 0.02$[(d)] | $0.61 \pm 0.03$[(g)] | $0.41 \pm 0.03$[(d)] |
| | | | | | $0.57 \pm 0.04$[(g)] | $0.41 \pm 0.13$[(f)] |
| | | | | | | $0.61 \pm 0.03$[(g)] |
| | | | | | | $0.500 \pm 0.008$[(h)] |

References: [(a)]Forrest et al. (1988); [(b)]Perryman et al. (1997); [(c)]Martín et al. (2000); [(d)]Lane et al. (2001); [(e)]Cutri et al. (2003);[(f)]Martín et al. (2006); [(g)]Simon et al. (2006); [(h)]Konopacky et al. (2010); [(i)]Dupuy et al. (2010);[(j)]This work.

Notes: (†)10.11 V Johnson magnitude converted from Hipparcos photometric system $H_p = 10.201 \pm 0.004$; [(*)]Unresolved GJ569B *I*-band magnitude in June 2009 at WHT; [(**)]Unresolved GJ569B *I*-band magnitude in July 2008 at NOT; (‡)Differential magnitude using the F814W filter in the HST which resembles the *I*-band.

error bars. Fig. 8 summarizes all the observations in the literature with our measurements in red. Our WHT astrometric value on June 2009 is nearly over imposed on the Keck AO-based observations by Dupuy et al. (2010) and Konopacky et al. (2010), the latter observved GJ569B within seven days after our observation. Overplotted we show the different orbits found in the literature together with our best Keplerian orbit to the same data plus our two new points. The orbital parameters of all these orbits are provided in Table 7 together with the total mass of the GJ569B system obtained by direct application of Kepler's third law. A very good agreement is found for the orbital parameters as well as for the estimated total mass of the system except from the value derived by Dupuy et al. (2010) (see discussion later in this section.)

In Table 7, in addition to the orbital parameters of the brown dwarf system, we also list the total mass estimates found in the literature together with our estimation which is consistent but slightly lower than previous results.

During the referee process of this work Dupuy et al. (2010) published a new set of values for the GJ569B system astrometry. As the authors remark, there has been a recent revision by van Leeuwen (2007) of the GJ569 Hipparcos parallax yielding a revised distance of $9.65 \pm 0.16$ pc instead of previous estimates of $9.81 \pm 0.16$ pc (Perryman et al. 1997); the impact of this new estimate of the GJ569 system distance is shown as an additional entry in Table 7. Dupuy et al. (2010) claim previous astrometric values obtained with the Keck AO facility in Lane et al. (2001); Zapatero Osorio et al. (2004); Simon et al. (2006) assumed a wrong plate scale. The same situation happens for the HST value on 2002 June 26th (which is also considered in Zapatero Osorio et al. 2005). Dupuy et al. (2010) reanalyze both the astrometric data in Simon et al. (2006) and the HST value on 2002 June 26th, and together with new 5 data points from January 2008 until May 2010 a new orbit is computed providing a mass estimate for the GJ569B system of $0.140^{+0.009}_{-0.008}$ $M_\odot$ . The comparison of the new orbit by Dupuy et al. (2010) against previous orbits in the literature is shown in a fraction of the orbit spanning the period April-June 2009 in Fig. 9.

**Table 6.** Astrometry of the binary system GJ569Ba-Bb.

| Date | Ref. | Teles-cope | In fit | Separation (arcsec) | PA (°) |
|---|---|---|---|---|---|
| 1999 Aug 29 | [(a)] | Keck | Yes | $0.101 \pm 0.001$ | $46.8 \pm 3$ |
| 2000 Feb 18 | [(b)] | Keck | Yes | $0.092 \pm 0.001$ | $98.2 \pm 3$ |
| 2000 Feb 25 | [(b)] | Keck | Yes | $0.090 \pm 0.001$ | $100.4 \pm 2$ |
| 2000 Jun 20 | [(b)] | Keck | Yes | $0.076 \pm 0.003$ | $138.6 \pm 2$ |
| 2000 Jul 4 | [(c)] | MMT | No | $0.078 \pm 0.003$ | $148 \pm 3$ |
| 2001 Mar 9 | [(c)] | SAO | No | $0.0896 \pm 0.0010$ | $321 \pm 1$ |
| 2001 Mar 10 | [(c)] | SAO | No | $0.0899 \pm 0.0010$ | $320 \pm 1$ |
| 2000 Aug 24 | [(b)] | Keck | Yes | $0.059 \pm 0.001$ | $178.4 \pm 2$ |
| 2001 Jan 9 | [(b)] | Keck | Yes | $0.073 \pm 0.002$ | $291.4 \pm 2$ |
| 2001 May 10 | [(b)] | Keck | Yes | $0.097 \pm 0.001$ | $341.1 \pm 3$ |
| 2001 Jun 28 | [(d)] | Keck | Yes | $0.1024 \pm 0.0012$ | $352.6 \pm 2$ |
| 2001 Sep 1 | [(d)] | Keck | Yes | $0.1033 \pm 0.0010$ | $9.7 \pm 2$ |
| 2002 Jun 26 | [(e)] | HST | No | $0.090 \pm 0.003$ | $94.4 \pm 1.2$ |
| 2003 Jul 11 | [(e)] | Subaru | No | $0.085 \pm 0.007$ | $319.8 \pm 4.4$ |
| 2004 Dec 24 | [(f)] | Keck | Yes | $0.0885 \pm 0.0048$ | $111.3 \pm 1.2$ |
| 2005 Feb 25 | [(f)] | Keck | Yes | $0.0798 \pm 0.0029$ | $133.7 \pm 0.7$ |
| 2008 Jan 16 | [(g)] | Keck | No | $0.0618 \pm 0.0007$ | $272.5 \pm 1.4$ |
| 2008 Jul 24 | [(h)] | NOT | Yes | $0.0981 \pm 0.0022$ | $351.8 \pm 1.4$ |
| 2009 Apr 29 | [(g)] | Keck | No | $0.1002 \pm 0.0006$ | $66.5 \pm 0.6$ |
| 2008 May 29 | [(g)] | Keck | No | $0.1005 \pm 0.0018$ | $75.0 \pm 1.7$ |
| 2009 Jun 4 | [(h)] | WHT | Yes | $0.0984 \pm 0.0011$ | $78.2 \pm 0.6$ |
| 2009 Jun 11 | [(i)] | Keck | Yes | $0.099 \pm 0.002$ | $79.4 \pm 0.2$ |
| 2010 Mar 22 | [(g)] | Keck | No | $0.0558 \pm 0.0003$ | $206.5 \pm 1.1$ |
| 2010 May 23 | [(g)] | Keck | No | $0.0599 \pm 0.0004$ | $268.1 \pm 0.4$ |

References: [(a)]Martín et al. (2000);[(b)]Lane et al. (2001); [(c)]Kenworthy et al. (2001);[(d)]Zapatero Osorio et al. (2004); [(e)]Zapatero Osorio et al. (2005); [(f)]Simon et al. (2006); [(g)]Dupuy et al. (2010); [(h)]This work; [(i)]Konopacky et al. (2010)

Column "In Fit" flags the data points used in our orbital solution. Data points flagged with NO correspond to new additions appeared during the referee stage.

**Table 7.** Orbital Parameters of GJ569Bab.

| Parameter | Zapatero04[(1)] | Simon06[(2)] | Konopacky10[(3)] | Dupuy10[(4)] | This Paper |
|---|---|---|---|---|---|
| Semimajor axis, a (mas) | $92 \pm 2$[(a)] | $90.4 \pm 0.7$ | $90.8 \pm 0.8$ | $95.6^{+1.1}_{-1.0}$ | $90.1 \pm 0.7$ |
| Eccentricity, e | $0.32 \pm 0.01$ | $0.312 \pm 0.007$ | $0.310 \pm 0.006$ | $0.316 \pm 0.005$ | $0.317 \pm 0.010$ |
| Inclination, i (°) | $34 \pm 2$ | $32.4 \pm 1.3$ | $33.6 \pm 1.3$ | $35.0 \pm 1.1$ | $30.0 \pm 1.6$ |
| Periapsis argument, $\omega$ (°) | $257 \pm 2$ | $256.7 \pm 1.7$ | $77.4 \pm 1.7$[(b)] | $257.9 \pm 2.0$ | $262.5 \pm 2.2$ |
| Ascending Node Longitude, $\Omega$ (°) | $321.5 \pm 2.0$ | $321.3 \pm 2.2$ | $144.8 \pm 1.9$[(b)] | $324.8 \pm 2.0$ | $313 \pm 4$ |
| Period, P(days) | $876 \pm 9$ | $863.7 \pm 4.2$ | $865.1 \pm 0.7$ | $864.0 \pm 1.1$ | $870 \pm 9$ |
| Total Mass, M($M_\odot$)[(c)] | $0.125 \pm 0.005$ | $0.125 \pm 0.007$ | $0.126 \pm 0.007$ | | $0.122 \pm 0.007$ |
| Total Mass, M($M_\odot$)[(d)] | $0.119 \pm 0.005$ | $0.119 \pm 0.007$ | $0.120 \pm 0.007$ | $0.140^{+0.009}_{-0.008}$ | $0.116 \pm 0.007$ |
| Epoch, T(yrs)[(e)] | $2000.758 \pm 0.008$ | $2000.754 \pm 0.007$ | $2003.150 \pm 0.005$ | $2010.255 \pm 0.004$ | |
| Epoch, T(yrs)[(f)] | $2010.36 \pm 0.10$ | $2010.22 \pm 0.05$ | $2010.260 \pm 0.008$ | $2010.255 \pm 0.004$ | $2010.263 \pm 0.012$ |

References: [(1)]Zapatero Osorio et al. (2004), [(2)]Simon et al. (2006), [(3)]Konopacky et al. (2010), [(4)]Dupuy et al. (2010)

Notes:

[(a)] In original paper quoted in AU. Converted to angular distance assuming GJ569 Hipparcos parallax $\pi = 0.10191 \pm 0.00167$ mas (Perryman et al. 1997).

[(b)] $\omega$ and $\Omega$ derived solely from astrometry results exhibit a 180°degeneracy which is broken when using spectroscopic data (e.g. radial velocities) such as in Zapatero Osorio et al. (2004), Simon et al. (2006) and Konopacky et al. (2010). However in the latter work there seems to appear again the degeneracy which was broken in Zapatero Osorio et al. (2004). The reason why such a degeneracy remains in Konopacky et al. (2010) is unknown to us.

[(c)] Total Mass derived using the GJ569A Hipparcos parallax $\pi = 0.10191 \pm 0.00167$ mas (Perryman et al. 1997) in original works by Zapatero Osorio et al. (2004), Simon et al. (2006) and Konopacky et al. (2010).

[(d)] Total Mass computed with the revised Hipparcos parallax $\pi = 0.10359 \pm 0.00172$ mas (van Leeuwen 2007) as pointed out in Dupuy et al. (2010). The total mass estimates in Zapatero Osorio et al. (2004), Simon et al. (2006) and Konopacky et al. (2010) scaled to the new parallax value.

[(e)] Epoch of periapsis appearing in original works.

[(f)] Epoch of periapsis propagated to fall within 2010 for the ease of comparison.

From theoretical models Dupuy et al. (2010) estimate the mass fraction parameter to be $q \simeq 0.87 \pm 0.02$, which agree very well with observational results in Zapatero Osorio et al. (2004) and (Konopacky et al. 2010). The new astrometric values in Dupuy et al. (2010) have not been considered in our orbital solution.

### 5.4 Constraining the binary nature of GJ569Ba.

From radial velocities Zapatero Osorio et al. (2004) assign individual masses of 0.071±0.011 $M_\odot$ and 0.054±0.011 $M_\odot$ for the GJ569Ba and GJ569Bb components, respectively. This is consistent with 0.073±0.008 $M_\odot$ and 0.053±0.006 $M_\odot$ by Konopacky et al. (2010) from radial velocity measurements. However, upon the discovery of the multiple nature of GJ569B by Martín et al. (2000), the possibility of GJ569Ba binarity was discussed. The reason argued in Martín et al. (2000) was the failure of theoretical models to fit the observational data with a single isochrone. The binary nature of GJ569Ba was again suggested in Kenworthy et al. (2001) on the basis of Bb being about half as bright as Ba while the GJ569B spectrum was fitted by a single M8.5 component and without evidence of reddening. Simon et al. (2006) gives further support to the Ba binarity when accounting from their estimated mass ratio $q = M_{Bb}/M_{Ba} = 0.19 \pm 0.13$ as derived from their radial velocities. Simon et al. (2006) suggest GJ569B is actually a triple system with Baa, Bab (i.e. the two suggested components of Ba) and Bb with nearly the same masses of around 0.04-0.05 $M_\odot$ . How does such a possibility fit into the larger collection of data since Simon et al. (2006)?

(i) The flux ratio evolution with wavelength is not consistent with a system of nearly three-equal mass objects. In such a case the flux ratio should remain constant while its evolution from I-band to L-band is clearly decreasing: $0.622 \pm 0.017$, $0.51 \pm 0.02$, $0.590 \pm 0.023$, $0.504 \pm 0.015$ and $0.49 \pm 0.03$ in I, J, H, K and L′ bands (the L′ measurement in Dupuy et al. 2010). This flux evolution is, however, consistent with Ba and Bb exhibiting slightly different radii (Ba larger than Bb) as suggested from theoretical models of BDs for the assumed masses of Ba and Bb and a slightly change in the effective temperature (Ba slightly hotter than Bb) consistent with the assigned spectral types to Ba and Bb in Lane et al. (2001). Notice also that the absence of a Li feature in the combined spectrum of GJ569B in (Zapatero Osorio et al. 2005) plays against the three-equal mass objects hypothesis: assuming the highest mass estimate for the GJ569B system of $0.140^{+0.009}_{-0.008}$ $M_\odot$ (Dupuy et al. 2010) would inevitably ensure the presence of Li features as all objects would be below the 0.060 $M_\odot$ threshold (Chabrier et al. 2000) but not such a feature was detected in Zapatero Osorio et al. (2005).

(ii) The age of the GJ569B is still an open issue with Simon et al. (2006) assigning a similar age to the Pleiades (∼ 120 Myr) and the rest of estimates in the literature proposing ages in the range 200-800 Myr. The (I-J) colors of 2.72±0.08 and 2.83±0.08 for the Ba and Bb components, respectively, do not match with what is expected from Pleiades objects with masses $\sim 0.04 - 0.05$ $M_\odot$ in the J vs. (I-J) Pleiades color-magnitude diagram in Bihain et al. (2006). Note that the older the system the more inconsistent the measured (I-J) colors of Ba and Bb with respect to masses as low as 0.04-0.05 $M_\odot$ . Note also that according to the the Lyon (Chabrier et al. 2000) and Tucson (Burrows et al. 1997) evolutionary models and for ages older than 250 Myr, objects with masses in the range 0.04-0.05 $M_\odot$ should exhibit spectral types in the L and T domain which is in contradiction with the M8.5-9.0 spectral types assigned to the unresolved GJ569B and resolved Ba and Bb components.

However, there is still the possibility that Ba is composed of two components, namely Baa and Bab, of different masses. For the purpose of the following discussion on the restrictions on the GJ569Ba binarity we assume the total mass estimate of $M_{Tot} = 0.140^{+0.009}_{-0.008}$ $M_\odot$ in Dupuy et al. (2010) and a mass ratio $q = 0.80 \pm 0.15$ which lies midway and consistently between the observed $q$ values in in Zapatero Osorio et al. (2004) and Konopacky et al. (2010), and the estimates by Dupuy et al. (2010)

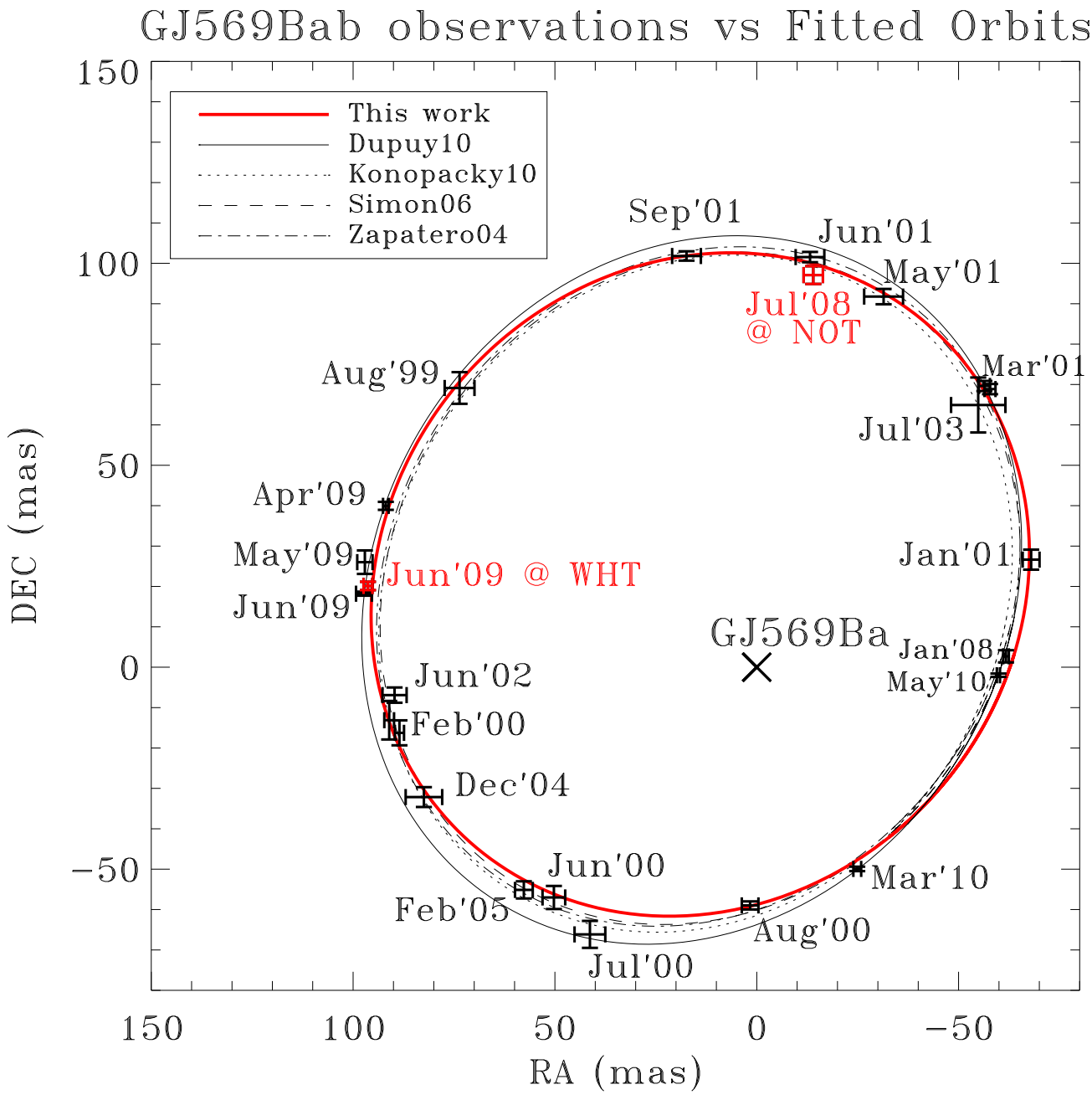


**Figure 8.** Compilation of astrometric data on the GJ569Bab pair with our points in red (see Table 6). Overplotted there are the different best-fit Keplerian orbits for the GJ569 multiple system found in the literature and derived in this work and whose orbital parameters are summarized in Table 7.

of $0.866^{+0.019}_{-0.014}$ and $0.886^{+0.021}_{-0.017}$ using the Lyon and Tucson evolutinary models. With these $M_{Tot}$ and $q$ values we have $M_{Ba} = 0.078 \pm 0.008$ $M_\odot$ and and $M_{Bb} = 0.062 \pm 0.008$ $M_\odot$ . A close look at the astrometric values reported in April-May 2009 by Dupuy et al. (2010), by June 2009 in Konopacky et al. (2010) and in this work are shown in Fig. 9, allowing us to place a constrain to the combination of mass and orbit semi-axis of a possible component Bab. From the above discussion we may safely assume that if GJ569Ba is binary then its most massive component must satisfy $0.060 < M_{Baa}/M_\odot < 0.086$ and $0 \leqslant M_{Bab}/M_\odot < 0.018$. Also, if Bab exists it should be either very faint and orbit around Baa with a semi-axis smaller than 0.5 AU (i.e. midpoint between Ba and Bb) and, using $M_{Ba} = 0.078 \pm 0.008$ $M_\odot$ , a possible orbital period T< 1.3 yr. The presence of Bab would induce a motion in the position of GJ569Baa which would reflect itself as a wobble of the orbit of GJ569Bb around the computed Keplerian orbits and with an amplitude $\alpha$ given by (e.g. Perryman 2000):

$$\alpha = \frac{M_P}{M_\star}\,\frac{a}{d} \qquad (2)$$

where $M_P$ and $M_\star$ are the masses of GJ569Bab and GJ569Baa, respectively, a is the Baa-Bab orbit semi-axis and d the distance

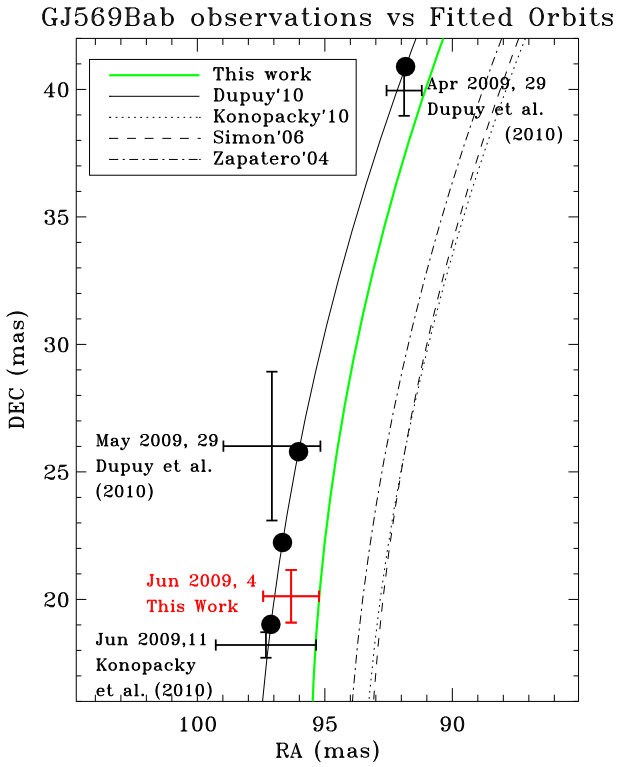


**Figure 9.** Zoomed part of orbit showing orbit in period April-June 2009 together with orbits in the literature and predicted positions in orbit model by Dupuy et al. (2010).

to GJ569 (i.e. $d \sim 10$ pc). Examining in detail the deviation of observed positions with respect to the Dupuy et al. (2010) orbit in the two month period depicted in Fig. 9 we place an upper limit $\alpha <$ 2.2 mas with $1\sigma$ confidence level. Using $M_{Baa} < 0.086$ $M_\odot$ we obtain the constrain $a{\cdot}M_{Bab} < 1.93$, with $M_{Bab}$ in units of $M_J$ (Jupiter mass) and a in AU. On the other hand we have placed an upper limit T< 1.3 yr on the period of Bab around of Baa. The residual rms of the observed positions on the period April 2009–May 2010 with respect the predicted positions allows to place an upper limit $\alpha < 1.9$ mas with $1\sigma$ confidence level and from here the constrain $a{\cdot}M_{Bab} < 1.68$. Adopting the former and more conservative constrain and since the minimum separation between GJ569Ba and GJ569Bb is $\sim 0.5$ AU, the widest possible orbit of Bab around Baa would be $< 0.25$ AU and we would have $M_{Bab} \lesssim 8$ $M_J$ and the closer Bab to Baa the higher the feasible value for $M_{Bab}$ . Given the range of masses under consideration and the distances between Baa and Bab, radial velocities studies of GJ569Ba should be able to shed further light into the existence of the Bab component.

## 6 CONCLUSIONS.

We have presented results showing the potential for high precision astrometry, differential photometry and high contrast imaging using a Lucky Imaging instrument coupled to an adaptive-optics system. Our results indicate that with 4-m class telescopes equipped with a moderately low order adaptive optics system it is possible to achieve angular resolutions better than 0.″1 in the I-band. This is comparable to what is achieved in the Ks band with the use of AO-systems at 8-10 m class telescopes. This work is part of an effort to determine the feasibility of a Lucky Imaging instrument to be coupled on the future AO system at the GTC telescope (GTCAO) and what the expectations in terms of high contrast imaging and angular resolution should be expected from such a combination.

Our work has focused on the observation of the GJ569 system which contains a benchmark brown dwarf binary. The application of our LM PSF fitting technique to the GJ569 image obtained with the WHT, where the GJ569B components are resolved, allows to achieve high precision relative photometry (to a few millimagnitudes) and astrometry (to a few mas) thanks to the availability of meaningful error bars associated to each pixel in the fitted image.

The potential for detection of faint companions has been addressed by looking at the $3\sigma$ detectability curves in Fig. 5. On the images directly from the frame selection procedure, we distinguish two regions in which the detectability behaves differently versus increasing the percentage of images being employed. In regions where the image is dominated by the wide swallow halo of the primary PSF, the detectability is improved by restricting the percentage of images being employed since in that way there is more energy in the core and less in the halo. At large distances from the primary, the image is dominated by background/detector noise and the detectability is improved by simply adding as many images as possible. On the wavelet-processed images, both in the inner and outer regions, we only see a benefit on the increase of the percentage of images used in the frame selection. With the wavelet-processed images we observe a magnitude gain in the inner region (1.7 magnitudes at 1″with respect to the non-processed image) but far away from the primary no net gain as those parts of the image are dominated by background/detector noise.

We have measured a differential magnitude at I band between GJ569Ba and GJ569Bb $\Delta m_{BaBb} = 0.622 \pm 0.017$. When used in conjunction of $\Delta m_{BaBb}$ in the J, H and K bands by previous works, fits well with the spectral determination of M8.5-M9 for the brown dwarf binary derived in the near-infrared by Lane et al. (2001). Our results in *I*-band and those in *J*, *H* and *K*-bands in Lane et al. (2001) clearly indicate that Ba is brighter than Bb. This together with the $I - J$ color favors a half subspectral class earlier for Ba than for Bb (see Fig. 6).

The astrometric quality achieved with FastCam allows to locate two new points on the GJ569Bb orbit around GJ569Ba. The orbits in the literature and the one derived including our points do not differ significantly and therefore the orbital parameters are in perfect agreement with those previously published, although our mass estimate of 0.116±0.007 $M_\odot$ using the updated Hipparcos parallax distance of 9.65±0.16 pc in van Leeuwen (2007). Our mass estimate of the multiple GJ569B system is somewhat smaller, but within error bars of previously published values except for the newly derived mass of $0.140^{+0.009}_{-0.008}$ $M_\odot$ in Dupuy et al. (2010). Our WHT data point on June 2009 falls within 1 sigma from the Dupuy et al. (2010) orbital solutions and our own orbital solution although our NOT data point on July 2008 is more consistent with previous orbital solutions in Zapatero Osorio et al. (2004); Simon et al. (2006); Konopacky et al. (2010). For a substantial refinement of the orbital parameters it would be necessary to sample the whole orbit with similar uncertainties as those derived from our observation at the WHT on June 2009.

The data available on the GJ569B system is consistent with a primary of $0.081 \pm 0.010$ $M_\odot$ and a secondary of $0.059 \pm 0.007$ $M_\odot$ . If Ba were a binary system then the Bab component would have a mass $< 0.018$ $M_\odot$ . A simple qualitative analysis on the deviations from a Keplerian orbit allows to place an upper limit to the product of mass and orbit semi-axis of this object.

**ACKNOWLEDGMENTS**

B.F. and L.L. are funded by the Spanish MICINN under the Consolider-Ingenio 2010 Program gran CSD2006-00070: First Science with the GTC (`http://www.iac.es/consolider-ingenio-gtc`). The 0.82-m IAC80 Telescope is operated on the island of Tenerife by the Instituto de Astrofisica de Canarias in the Spanish Observatorio del Teide. This research has made use of the Washington Double Star Catalog maintained at the U.S. Naval Observatory. We thank the referee María Rosa Zapatero Osorio for many insightful discussions which have substantially improved the contents of the orginal manuscript. We also wish to thank to the IAC teams lead by Emilio Cadavid and Vicente Sánchez and all the ING staff, and specially to Chris Benn and Tibor Agocs, for their very precious help during the setup and observations with FastCam at the WHT.

**References**

Baldwin J. E., Tubbs R. N., Cox G. C., Mackay C. D., Wilson R. W., Andersen M. I., 2001, A&A, 368, L1

Benn C., 2006, New Astronomy Reviews, 49, 625

Bevington P. D., 1992, Data Reduction and Error Analysis for the Physicial Sciences, 2nd edn. McGraw-Hill, New York

Bihain G., Rebolo R., Béjar V. J. S., Caballero J. A., Bailer-Jones C. A. L., Mundt R., Acosta-Pulido J. A., Manchado Torres A., 2006, A&A, 458, 805

Burrows A., Marley M., Hubbard W. B., Lunine J. I., Guillot T., Saumon D., Freedman R., Sudarsky D., Sharp C., 1997, ApJ, 491, 856

Carpenter J. M., 2001, AJ, 121, 2851

Chabrier G., Baraffe I., Allard F., Hauschildt P., 2000, ApJ, 542, 464

Cutri R. M., Skrutskie M. F., van Dyk S., Beichman C. A., Carpenter J. M., Chester T., Cambresy L., Evans T., Fowler J., Gizis J., Howard E., Huchra J., Jarrett T., Kopan E. L., Kirkpatrick J. D., 2003, 2MASS All Sky Catalog of point sources.

Dupuy T. J., Liu M. C., Bowler B. P., Cushing M. C., Helling C., Witte S., Hauschildt P., 2010, ApJ, 721, 1725

Dupuy T. J., Liu M. C., Ireland M. J., 2009, ApJ, 692, 729

Forrest W. J., Shure M., Skrutskie M. F., 1988, ApJ, 330, L119

Fried D. L., 1978, JOSA, 68, 1651

Fuensalida J. J., García-Lorenzo B. M., Castro J., Chueca S., Delgado J. M., González-Rodríguez J. M., Hoegemann C. K., Reyes M., Verde M., Vernin J., 2004, in Schäfer K. P., Comerón A., Carleer M. R., Picard R. H., Sifakis N. I., eds, Remote Sensing of Clouds and the Atmosphere IX Vol. 5572 of Proc. SPIE, Statistics of atmospheric parameters for multiconjugated adaptive optics for the Observatorio del Roque del los Muchachos. pp 1–9

Gladysz S., Christou J., Law N., Dekany R., Redfern M., Mackay C., 2008, in Hubin N., Max C. E., Wizinowich P. L., eds, Adaptive Optics Systems Vol. 7015 of Proc. SPIE, Lucky imaging and speckle discrimination for the detection of faint companions with adaptive optics

Kenworthy M., Hofmann K., Close L., Hinz P., Mamajek E., Schertl D., Weigelt G., Angel R., Balega Y. Y., Hinz J., Rieke G., 2001, ApJ, 554, L67

Kervella P., Verhoelst T., Ridgway S. T., Perrin G., Lacour S., Cami J., Haubois X., 2009, A&A, 504, 115

Kirkpatrick J. D., McCarthy Jr. D. W., 1994, AJ, 107, 333

Konopacky Q. M., Ghez A. M., Barman T. S., Rice E. L., Bailey J. I., White R. J., McLean I. S., Duchêne G., 2010, ApJ, 711, 1087

Labadie L., Rebolo R., Femenía B., Villó I., Díaz-Sánchez A., Oscoz A., López R., Pérez J. A., Pérez A., Hildebrandt S. R., Béjar V., José Piqueras J., Rodríguez L. F., 2010, in Society of Photo-Optical Instrumentation Engineers (SPIE) Conference Series Vol. 7735 of Proc. SPIE, High spatial resolution and high contrast optical speckle imaging with FASTCAM at the ORM

Labadie L., Rebolo R., Villo I., Perez-Prieto J. A., Perez-Garrido A., Hildebrandt S. R., Femenia B., Diaz-Sanchez A., Bejar V. J. S., Oscoz A., Lopez R., Piqueras J., Rodriguez L. F., 2010, ArXiv e-prints

Landolt A. U., 1992, AJ, 104, 340

Lane B. F., Zapatero Osorio M. R., Britton M. C., Martín E. L., Kulkarni S. R., 2001, ApJ, 560, 390

Law N. M., Mackay C. D., Baldwin J. E., 2006, A&A, 446, 739

Law N. M., Mackay C. D., Dekany R. G., Ireland M., Lloyd J. P., Moore A. M., Robertson J. G., Tuthill P., Woodruff H. C., 2009, ApJ, 692, 924

Liebert J., Gizis J. E., 2006, PASP, 118, 659

Martín E. L., Brandner W., Bouy H., Basri G., Davis J., Deshpande R., Montgomery M. M., 2006, A&A, 456, 253

Martín E. L., Koresko C. D., Kulkarni S. R., Lane B. F., Wizinowich P. L., 2000, ApJ, 529, L37

Masciadri E., Raga A., 2004, ApJ, 611, L137

Myers R. M., Longmore A. J., Benn C. R., Buscher D. F., Clark P., Dipper N. A., Doble N., Doel A. P., Dunlop C. N., Gao X., Gregory T., Humphreys R. A., Ives D. J., Østensen R., 2003, in Wizinowich P. L., Bonaccini D., eds, Adaptive Optical System Technologies II Vol. 4839 of Proc. SPIE, NAOMI adaptive optics system for the 4.2m William Herschel telescope. pp 647–658

Oscoz A., Rebolo R., López R., Pérez-Garrido A., Pérez J. A., Hildebrandt S., Rodríguez L. F., Piqueras J. J., Villó I., González J. M., Barrena R., Gómez G., García A., Montañés P., 2008, in McLean I. S., Casali M. M., eds, Ground-based and Airborne Instrumentation for Astronomy II. Vol. 7014 of Proc. SPIE, FastCam: a new lucky imaging instrument for medium-sized telescopes. pp 701447–1 – 701447–12

Perryman M. A. C., 2000, Reports on Progress in Physics, 63, 1209

Perryman M. A. C., Lindegren L., Kovalevsky J., Hoeg E., Bastian U., Bernacca P. L., Crézé M., Donati F., Grenon M., van Leeuwen F., van der Marel H., Mignard F., Murray C. A., 1997, A&A, 323, L49

Simon M., Bender C., Prato L., 2006, ApJ, 644, 1183

Tubbs R. N., Baldwin J. E., Mackay C. D., Cox G. C., 2002, A&A, 387, L21

van der Marel R. P., Gerssen J., Guhathakurta P., Peterson R. C., Gebhardt K., 2002, AJ, 124, 3255

van Leeuwen F., ed. 2007, Hipparcos, the New Reduction of the Raw Data Vol. 350 of Astrophysics and Space Science Library

Wycoff G. L., Mason B. D., Urban S. E., 2006, AJ, 132, 50

Zapatero Osorio M. R., Lane B. F., Pavlenko Y., Martín E. L., Britton M., Kulkarni S. R., 2004, ApJ, 615, 958

Zapatero Osorio M. R., Martín E. L., Lane B. F., Pavlenko Y., Bouy H., Baraffe I., Basri G., 2005, Astronomische Nachrichten, 326, 948